5-1-2023

Devouring the Milky Way Satellites: Modeling Dwarf Galaxies with Galacticus

Sachi Weerasooriya
Texas Christian University

Mia Sauda Bovill
Texas Christian University

Andrew Benson
Carnegie Observatories

Alexi M. Musick
San Jose State University, alexi.musick@sjsu.edu

Massimo Ricotti
University of Maryland, College Park

Recommended Citation

Sachi Weerasooriya, Mia Sauda Bovill, Andrew Benson, Alexi M. Musick, and Massimo Ricotti. "Devouring the Milky Way Satellites: Modeling Dwarf Galaxies with Galacticus" *Astrophysical Journal* (2023). https://doi.org/10.3847/1538-4357/acc32b

The Astrophysical Journal, 948:87 (14pp), 2023 May 10 https://doi.org/10.3847/1538-4357/acc32b

Devouring the Milky Way Satellites: Modeling Dwarf Galaxies with Galacticus

Sachi Weerasooriya[1], Mia Sauda Bovill[1], Andrew Benson[2], Alexi M. Musick[3], and Massimo Ricotti[4]
[1] Department of Physics and Astronomy, Texas Christian University, Fort Worth, TX 76109, USA
[2] Carnegie Observatories, 813 Santa Barbara Street, Pasadena, CA 91101, USA
[3] Department of Physics and Astronomy, San José State University, San José, CA 95192, USA
[4] Department of Astronomy, University of Maryland, College Park, MD 20742, USA
Received 2022 August 16; revised 2023 February 15; accepted 2023 March 8; published 2023 May 10

Abstract

Dwarf galaxies are ubiquitous throughout the universe and are extremely sensitive to various forms of internal and external feedback. Over the last two decades, the census of dwarf galaxies in the Local Group and beyond has increased markedly. While hydrodynamic simulations (e.g., FIRE II, Mint Justice League) have reproduced the observed dwarf properties down to the ultrafaints, such simulations require extensive computational resources to run. In this work, we constrain the standard physical implementations in the semianalytic model Galacticus to reproduce the observed properties of the Milky Way satellites down to the ultrafaint dwarfs found in the Sloan Digital Sky Survey. We run Galacticus on merger trees from our high-resolution *N*–body simulation of a Milky Way analog. We determine the best-fit parameters by matching the cumulative luminosity function and luminosity–metallicity relation from both observations and hydrodynamic simulations. With the correct parameters, the standard physics in Galacticus can reproduce the observed luminosity function and luminosity–metallicity relation of the Milky Way dwarfs. In addition, we find a multidimensional match with half-light radii, velocity dispersions, and mass to light ratios at $z = 0$ down to $M_V \leqslant -6$ ($L \geqslant 10^4\ L_\odot$). In addition to successfully reproducing the properties of the $z = 0$ Milky Way satellite population, our modeled dwarfs have star formation histories that are consistent with those of the Local Group dwarfs.

Unified Astronomy Thesaurus concepts: Dwarf galaxies (416)

1. Introduction

Dwarf galaxies are the most common type of galaxy in the universe (Ferguson & Binggeli 1994), and their shallow potential wells make them extremely sensitive to internal and external feedback (e.g., Dekel & Silk 1986; Thoul & Weinberg 1996; Benson et al. 2002; Okamoto et al. 2010). Thus, they are excellent probes of both dark matter (e.g., Polisensky & Ricotti 2011) and internal/external environmental physical processes.

In the last 15 yr, the census of dwarf galaxies in the Local Group has more than doubled due to the Sloan Digital Sky Survey (SDSS; Albareti et al. 2017; Aguado et al. 2019), the Dark Energy Survey (DES; Abbott et al. 2018), and PAndAS (Martin et al. 2016). In addition, ongoing and upcoming surveys are pushing the frontiers of observational studies of dwarf galaxies beyond the Local Group. These include, among others, targeted surveys of Centaurus A (Crnojevic 2020), M81/M82 (Sorgho et al. 2019), and wider surveys such as SAGA (Geha et al. 2017; Mao et al. 2021).

In concert with our increased understanding of the observational properties of dwarf galaxies, theoretical studies of the fossils of the first galaxies (Bovill & Ricotti 2009; Ricotti et al. 2016; Wheeler et al. 2019) and of dwarf satellites around the Milky Way using hydrodynamical simulations have come of age (Applebaum et al. 2021; Wetzel et al. 2023). Hopkins et al. (2014, 2018) and Wetzel et al. (2023) simulated a Milky Way analog, resolving star formation physics down to low-mass dwarfs ($M_V < -8$, $M_* \geqslant 1.6 \times 10^3\ M_\odot$). The Mint Justice League simulations have reproduced properties of the Milky Way satellite system, including the half-light radii, velocity dispersion, and metallicity of the ultrafaints (Applebaum et al. 2021).

Despite their success, high-resolution hydrodynamical simulations of Milky Way analogs require extensive computational resources. As our observational sample of dwarf galaxies expands beyond the Local Group, there is a need to simulate dwarf satellite systems in a wider range of environments than can be currently explored by hydrodynamical simulations. Moreover, exploration of the astrophysics involved in any part of the baryon cycle is crucial to understanding how sensitive the feedback mechanisms in dwarf galaxies are to their local environment. Due to their high computational costs, hydrodynamical simulations are not the ideal tool for this work.

In semianalytic models (SAMs) the baryonic physics is approximated by a set of interconnected differential equations to model the baryonic evolution of galaxies through cosmic time. This is an efficient way of modeling galaxies (e.g., Henriques et al. 2009; Benson & Bower 2010; Bower et al. 2010) and permits rapid modeling of dwarf galaxies in a range of environments. While SAMs are computationally efficient and use relatively straightforward physics, formulated via simple ordinary differential equations (ODEs), their underlying assumptions and simplifications must be tested against more sophisticated hydrodynamic simulations.

Various studies have used SAMs to model galaxies. These analytic models were first proposed by White & Rees (1978), and advanced by White & Frenk (1991), Kauffmann et al. (1993), Somerville & Primack (1999), Cole et al. (2000), Hatton et al. (2003), Monaco et al. (2007), Somerville & Davé (2015), and others. While the first SAMs were built on Extended Press–Schechter merger trees (Press &

Schechter 1974), they can now be applied to merger trees from *N*-body simulations (e.g., Kauffmann et al. 1999; Helly et al. 2003).

Previous studies modeling dwarf galaxies with SAMs include Li et al. (2010), Font et al. (2011), Starkenburg et al. (2013), Lu et al. (2017), Pandya et al. (2020), Bose et al. (2020), Jiang et al. (2021), and Chen et al. (2022). Macciò et al. (2010) reproduced the luminosity function of the Milky Way (MW) satellites down to the ultrafaints. Starkenburg et al. (2013) reproduced the luminosity function and the luminosity–metallicity relation down to $M_V < -5$. They also reproduce the star formation histories (SFHs) of some satellites, although models do not match all of their observed properties. Jiang et al. (2021) used `SatGen` to produce a statistical sample of Local Group satellites. Bose et al. (2020) used the Durham SAM with high-resolution *N*-body simulations to explore the relation between abundance and assembly history of the host. These authors have also reproduced the radial distribution of satellite galaxies. Pandya et al. (2020) tested the Santa-Cruz SAM (Somerville & Primack 1999) against the FIRE-II cosmological simulations. Although their stellar–halo mass relations and stellar mass assembly histories agree well with FIRE-II, interstellar medium (ISM) masses agree only for higher-mass halos. In order to reproduce gas accretion efficiencies of FIRE-II dwarfs, they implement a mass-dependent preventative feedback model to suppress accretion of gas into halos. Note that "preventative feedback" here means preventing accretion of gas onto halos via stellar feedback (Lu et al. 2017; Pandya et al. 2020). However, details between implementations in the Santa Cruz SAM (Pandya et al. 2020) and the SAM by Lu et al. (2017) vary. The recent study by Chen et al. (2022) has reproduced the stellar mass to halo mass relation of the MW satellites at $z = 0$ down to the ultrafaints while providing a framework to study stellar properties and SFHs of metal-poor stars.

In this work, we will determine whether the Galacticus SAM (Benson 2012), run on high-resolution merger trees from a cosmological *N*-body simulation, can reproduce the properties of the Milky Way dwarfs.

In Section 2 we describe our simulation and the process of constraining Galacticus. In Section 3, we present predictions from the constrained Galacticus parameters down to ultrafaint dwarf scales. Next, we discuss our results and limitations in Section 4, and finally summarize our findings in Section 5.

2. Simulations

We run an *N*-body simulation of a Milky Way analog from $z = 150$ to $z = 0$ with WMAP9 cosmology ($\sigma_8 \sim 0.821$, $H_0 \sim 70.0\,\mathrm{km\,s^{-1}\,Mpc^{-1}}$, $\Omega_b \sim 0.0463$, $\Omega_\Lambda \sim 0.721$). Initial conditions were generated with MUSIC (Hahn & Abel 2011), and the simulation was run with Gadget 2 (Springel 2005). The simulation is analyzed with both the AMIGA (Knollmann & Knebe 2009) and Rockstar (Behroozi et al. 2013a) halo finders following the virial overdensity from Bryan & Norman (1998). Merger trees are generated using the Consistent Trees (Behroozi et al. 2013b).

We select an isolated Milky Way analog from a $50\,\mathrm{Mpc}\,h^{-1}$ box with $N_{\rm eff} = 256^3$ run from $z = 150$ to $z = 0$, resolving the Milky Way candidates at $z = 0$ with $N > 1000$ particles. Our isolation criteria is an $M_{\rm vir} \sim 10^{12} M_\odot$ halo, with no halos greater than $M_{\rm vir} \sim 10^{12}\,M_\odot$ within $3\,\mathrm{Mpc}\,h^{-1}$ at $z = 0$. We select an MW analog with $M_{\rm vir} \sim 1.8 \times 10^{12}\,M_\odot$ ($M_{\rm vir} \sim 1.2 \times 10^{12}\,M_\odot\,h^{-1}$) following the above conditions. Note that our simulation has only one such MW analog with the surrounding environment. The effects of small number statistics will be minimized if multiple zoomed-in simulations were run. However, such exploration is the subject of a future work. Once a Milky Way analog is identified at $z = 0$, we rerun a dark-matter-only zoom-in simulation centered on that chosen halo. The high-resolution region at $z = 150$ is defined by the particles within $5\,R_{\rm vir}$ from the Milky Way analog at $z = 0$. The highest-resolution region has $N_{\rm eff} = 4096^3$, resolving $M_{\rm vir} \sim 10^7\,M_\odot$ halos with at least 100 particles and softening of $\epsilon = 200\,\mathrm{pc}$ (physical units).

All simulations described in this work were run on the Maryland High Performance Computer Cluster Deepthought 2[5].

We then run Galacticus on the resulting merger trees. Note that most dark matter halo properties (total mass, Navarro–Frenk–White, NFW, scale length) used in Galacticus are preset from the *N*-body trees with the exception of halo spins. Halo spins are typically not well-measured in halos with fewer than of the order of 40,000 particles (Benson 2017a). In addition, cosmological simulations can also suffer from overmerging due to inadequate softening. For example, van den Bosch & Ogiya (2018) recommend subhalos be simulated with at least 10^6 particles with softening length 0.03 times their NFW scale radius in order to properly track their dynamics and disruption.

2.1. Constraining Galacticus with the Milky Way Satellites

We determine the set of Galacticus' parameters that best fit the observed luminosity function and the luminosity–metallicity relation for dwarf satellites of the Milky Way. We compare the galaxy models to the updated McConnachie (2012) table as of 2021 January.[6] In addition, we have added a few satellites from Drlica-Wagner et al. (2020) that are missing from McConnachie (2012). Note that we do not do any formal fitting. Instead, we run a grid of models and choose the ones that produce the best match based on a "by-eye" judgement. We start from Galacticus' standard set of parameters[7] constrained to match the baryonic physics of massive galaxies. Unless mentioned below, we use the parameters given in the file above.

The parameters for massive galaxies have been calibrated to observational data sets, including the stellar mass halo relation of Leauthaud et al. (2012) and its scatter from More et al. (2009), the $z < 0.06$ stellar mass function of galaxies from the GAMA survey (Baldry et al. 2012), the $z = 2.5 - 3.0$ stellar mass functions of galaxies from the ULTRAVISTA survey (Muzzin et al. 2013), the $z = 0$ H I mass function of galaxies from the ALFALFA survey (Martin et al. 2010), the $z = 0$ black hole mass–bulge mass relation of Kormendy & Ho (2013), size distributions of SDSS galaxies from Shen et al. (2003), Hα luminosity functions from HiZELS (Sobral et al. 2013) and GAMA (Gunawardhana et al. 2013), *g*- and *r*-band luminosity functions of SDSS galaxies (Montero-Dorta & Prada 2009), the gas-phase mass–metallicity relation (Blanc et al. 2019), and the morphological fraction as a function of stellar mass from GAMA (Moffett et al. 2016).

[5] http://hpcc.umd.edu

[6] https://www.cadc-ccda.hia-iha.nrc-cnrc.gc.ca/en/community/nearby/

[7] github.com/galacticusorg/galacticus/blob/889ab5d347001c9623d74609b51850c080829f96/parameters/baryonicPhysicsConstrained.xml

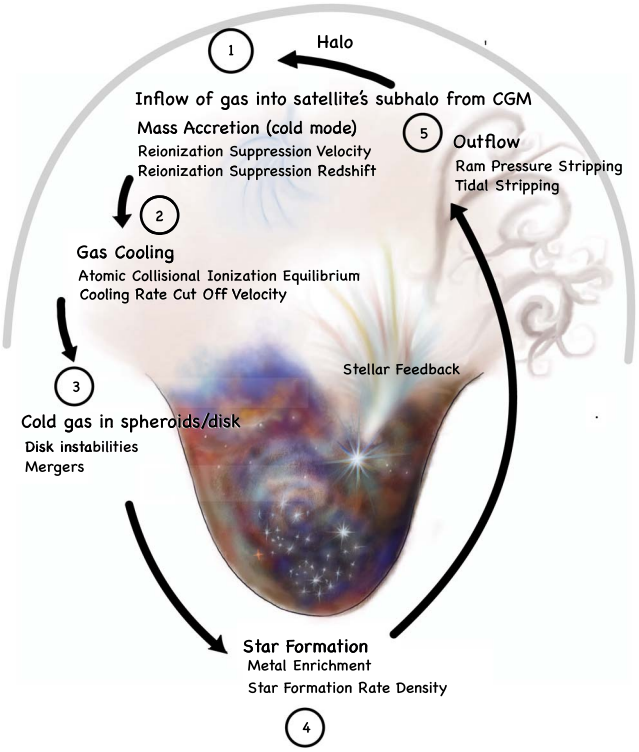

Figure 1. Diagram of the baryon cycle. Stage 1: inflow of gas into the satellite's subhalo from the circumgalactic medium (CGM) of the parent MW halo. Stage 2: cooling of CGM gas in the subhalo and inflow to the subhalo center to form a galaxy. Stage 3: the accreted material then provides gas for spheroid/disks. Stage 4: cold gas forms stars. Stage 5: finally, some of the gas within the satellite's subhalo flows back into the MW halo's diffuse CGM due to tidal stripping, ram pressure stripping, and supernova feedback.

In the following sections, we discuss how we systematically modify the parameters to optimize the baryon cycle (Figure 1) and reproduce the observed luminosities and metallicities of the Milky Way satellites. We divide our discussion of the modified parameters into two subsets, those that are well constrained by astrophysics governing dwarf galaxies or their properties (Section 2.1.1), and those that are not (Section 2.1.2).

2.1.1. Parameters with Astrophysical Priors

We begin with parameters whose values are determined, or at least limited, by the astrophysics governing dwarf galaxies or the derived properties of the Milky Way.

Cooling velocity: atomic hydrogen cooling is suppressed for low-mass halos with virial temperatures below $\sim 10^4$ K. This is known as the atomic hydrogen cooling limit, which corresponds to a virial velocity of $\sim$16 km s^{-1} (Fitts et al. 2017; Graus et al. 2019). To suppress star formation in the least-massive halos, Galacticus uses a minimum $v_{\rm vir}$ below which gas in a halo will be unable to cool and form stars ($v_{\rm cooling}$). In this work, we choose $v_{\rm cooling}$ values to approximate this atomic cooling limit since gas accretion onto and star formation in halos below the atomic cooling limit is inefficient. Similar thresholds have been used in several high-resolution hydrodynamic simulations (Sawala et al. 2016; Benítez-Llambay et al. 2017; Fitts et al. 2017; Macciò et al. 2017; Munshi et al. 2021). Note that the collisional ionization equilibrium cooling function does not drop entirely to zero below this threshold due to contributions from metal cooling. Modeling star formation in halos below the atomic cooling threshold requires accounting for the stochastic effects of H_2 cooling, and is beyond the scope of the current work. Therefore, we only consider halos that are above the atomic cooling limit and narrow our choices of velocities ($v_{\rm cooling} = 15$–20 km s^{-1}).

Reionization redshift: the redshift of reionization for the Milky Way and its local environment is set at $z_{\rm reion} = 9$. This value falls within the range of reionization redshifts calculated by previous works (Bullock et al. 2000; Gnedin 2000; Alvarez et al. 2009; Busha et al. 2010; Iliev et al. 2011; Spitler et al. 2012; Ocvirk et al. 2013; Li et al. 2014; Aubert et al. 2018).

Filtering velocity: during and after reionization, the reheating of the intergalactic medium suppresses the accretion of gas onto low-mass halos below the filtering mass (Ricotti & Gnedin 2005). Galacticus parameterizes this with the reionization suppression velocity $v_{\rm filter}$. Therefore, accretion of gas is suppressed in halos with $v_{\rm virial} \leqslant v_{\rm filter}$. Note that in this case accretion is completely turned off. When modeling the effects of reionization on halos across a range of redshifts, this criterion is the superior choice (compared to, for example, a halo-mass-based criterion) as the virial velocity of a halo is a direct and redshift-independent measure of the depth of the potential well.

Star formation law in disks: we calculate the star formation rate density for the disks using the model of Blitz & Rosolowsky (2006). We choose this prescription because it is based on the astrophysics of molecular hydrogen as opposed to fits of observed data from more-massive galaxies (Kennicutt 1998; Shi et al. 2011). This method describes a star formation prescription based on hydrostatic pressure. It uses the linear relation between pressure and the ratio of molecular to atomic gas in galaxies. The star formation rate surface density is computed by

$$\dot{\Sigma}_*(R) = \nu_{\rm SF}(R)\Sigma_{\rm H_2,disk}(R). \quad (1)$$

Here the star formation frequency is given by $\nu_{\rm SF}(R) = \nu_{\rm SF,0}\left[1 + \left(\frac{\Sigma_{\rm H\,I}}{\Sigma_0}\right)^q\right]$, where Σ_0 is the critical surface density for formation of molecules, and q is an exponent. Note that the star formation efficiency is suppressed in "subcritical" regions where $\Sigma_{\rm H\,I} < \Sigma_0$. The surface density of molecular gas is given by

$$\Sigma_{\rm H_2} = \left(\frac{P_{\rm ext}}{P_0}\right)^\alpha \Sigma_{\rm H\,I}, \quad (2)$$

where P_0 is the characteristic pressure, and α is the pressure exponent (we use $\alpha = 0.92$ as suggested by Blitz & Rosolowsky 2006). External hydrostatic pressure within a gas cloud in the disk is calculated by,

$$P_{\rm ext} = \frac{\pi}{4} G\Sigma_{\rm gas}\left[\Sigma_{\rm gas} + \left(\frac{\sigma_{\rm gas}}{\sigma_*}\right)\Sigma_*\right], \quad (3)$$

where $\Sigma_* = \sqrt{\pi G h_* \Sigma_*}$ is the surface density of the stars, and h_* is the disk scale height. Note that this equation is valid only under the condition $\Sigma_* \gg \Sigma_{\rm gas}$. We do not vary any parameters for this prescription.

Star formation in spheroids: star formation rates in spheroids are calculated using dynamical times with the same parameters as for the best fit to the more-massive galaxies. The timescale

for star formation is given by

$$\tau_* = \epsilon_*^{-1}\tau_{\rm dynamical}\left(\frac{V}{200\ \ {\rm km\ s^{-1}}}\right)^{\alpha_*}, \quad (4)$$

where ϵ_* and α_* are input parameters, and $\tau_{\rm dynamical} = r/V$, where r and V are the characteristic radius and velocity of the spheroidal component, respectively. This timescale cannot fall below a minimum value of 7.579 Gyr. Gas can be added to the spheroid via mergers and disk instabilities. In a major merger, both galaxies are destroyed and a new spheroid is created with combined gas from destroyed galaxies, while in a minor merger, gas from the merging satellite is added to the more-massive spheroid. Note that we do not vary any parameters for this method. We use the default values for each parameter given in Galacticus documentation.

Accretion mode onto halos: gas can accrete onto halos in one of two "modes": "cold" and "hot." In "hot-mode" accretion, all accreted gas is shock heated to the virial temperature of the halo. Although this model describes the process of accretion well for higher-mass halos, gas accretion in low-mass halos (dwarfs) is never shock heated to the virial temperature (Fardal et al. 2001; Kereš et al. 2005, 2009). Studies such as Kereš et al. (2005, 2009) show that "cold-mode" gas accretion dominates low-mass galaxies (i.e., $<10^{10.3}\,M_\odot$) while "hot-mode" accretion of gas occurs in higher-mass systems. In "cold-mode" accretion, the gas accreted never forms a hydrostatic halo, and so does not need to cool and radiate its thermal energy before flowing into the galaxy. It instead flows into the galaxy on the order of the dynamical time. Therefore, we implement "cold-mode" accretion onto low-mass halos, "hot-mode" accretion onto high-mass halos, and a mixture of both to intermediate-mass halos. The transition between two modes is determined by two "shock" parameters.

According to Birnboim & Dekel (2003) and Benson & Bower (2010), the cold-mode fraction is defined by

$$f_{\rm cold} = (1 + r^{\frac{1}{\delta}})^{-1}, \quad (5)$$

where δ is the shock stability transition width, $r = \epsilon_{\rm crit}/\epsilon$ and $\epsilon = r_{\rm s}\Lambda\rho_s v_s^3$ where $r_{\rm s}$ is the accretion shock radius (set to the virial radius), Λ is the post-shock cooling function, $\rho_{\rm s}$ and $v_{\rm s}$ are pre-shock density and velocity (at the virial radius), respectively, and $\epsilon_{\rm crit}$ is the accretion shock stability threshold. Here, the pre-shock density is defined by

$$\rho_s = \frac{\gamma-1}{\gamma+1}\frac{3}{4\pi}\frac{\Omega_{\rm b}}{\Omega_{\rm m}}\frac{M}{r_{\rm s}^3}\left[1 + \frac{(\alpha+3)(10+9\pi)}{4}\right]^{-1}, \quad (6)$$

where M is the total halo mass, $\gamma = 5/3$ is the adiabatic index of gas, and α is the exponent that corresponds to initial density perturbation (Birnboim & Dekel 2003). Note that while we choose the cold-mode method for accretion, the parameters above are not variable and are set by internal calculations.

2.1.2. Parameters without Astrophysical Priors

We next describe the parameters that are unconstrained by the underlying astrophysics of either dwarf galaxies or the Milky Way. Ram pressure and tidal stripping were constrained by comparisons to the observed and simulated (Applebaum et al. 2021; Shipp et al. 2022) luminosity functions of the Milky Way satellites. The physics of star formation feedback is constrained to best fit the slope and scatter of the luminosity–metallicity relation.

Ram Pressure Stripping: We use the model of Font et al. (2008) to model ram pressure stripping of hot halo gas in our dwarf galaxies, as this method sets a physical radius within the dwarf galaxy halo. The ram pressure stripping radius of Font et al. (2008) is a solution to

$$\alpha\frac{GM_{\rm satellite}(r_{\rm rp})\rho_{\rm hot,satellite}(r_{\rm rp})}{r_{\rm rp}} = \mathcal{F}_{\rm ram,hot,host}, \quad (7)$$

where $\mathcal{F}_{\rm ram,hot,host}$ is the ram pressure force due to the host halo, geometric factor $\alpha = \beta_{\rm ram}\mathcal{F}_{\rm hot,host}/F_{\rm gravity}$, and the total mass of the satellite within radius r, $M_{\rm satellite}(r)$. $\rho_{\rm hot,satellite}$ is the hot halo density profile of the node's host at pericenter radius $r_{\rm rp}$. The ram pressure force due to the hot halo is defined by

$$\mathcal{F}_{\rm ram,hot,host} = \rho_{\rm hot,host}(r)v^2(r). \quad (8)$$

The mass-loss rate in disks is computed using the equation

$$\dot{M}_{\rm gas,disk} = \min\left(\frac{\beta_{\rm ram}\mathcal{F}_{\rm hot,host}}{2\pi G\Sigma_{\rm gas}(r_{1/2})\Sigma_{\rm total}(r_{1/2})}, R_{\rm max}\right) \times \frac{M_{\rm gas,disk}}{\tau_{\rm dyn,disk}}, \quad (9)$$

where $\beta_{\rm ram}$ is the ram pressure stripping efficiency, which scales the mass loss in the disk, $\Sigma_{\rm gas}(r)$ is the gas surface density in the disk, $\Sigma_{\rm total}(r)$ is the total surface density in the disk, $r_{1/2}$ is the disk half mass–radius, $M_{\rm gas,disk}$ is the total gas mass in the disk, $\tau_{\rm dyn,disk}$ is the dynamical time in the disk, $R_{\rm max}$ determines the maximum rate of gas mass lost, and G is the gravitational constant.

In spheroids, the rate of gas mass loss is calculated using

$$\dot{M}_{\rm gas,sph} = -\max(\alpha, R_{\rm max})M_{\rm gas}/\tau_{\rm sph}, \quad (10)$$

where $M_{\rm gas}$ is the mass of gas in spheroid, and $\tau_{\rm sph}$ is the dynamical time of the spheroid. The gravitational restoring force at half mass–radius is given by

$$F_{\rm gravity} = \frac{4}{3}\rho_{\rm gas}(r_{1/2})\frac{GM_{\rm total}(r_{1/2})}{r_{1/2}}.$$

Tidal Stripping: There is evidence for tidal stripping in dwarf satellites embedded in the scatter of the halo mass–stellar mass relation (Jackson et al. 2021) and the presence of tidal streams and debris (Bullock & Johnston 2005). Previous studies have shown that more dark matter must be stripped in order for stripping of stars to occur in galaxies with smaller disks (Peñarrubia et al. 2008; Smith et al. 2013). Simulations suggest that stars in dwarf spheroids are only stripped after 80%–90% of the dark matter is stripped (Smith et al. 2013). In addition, galaxies that lose 80% of dark matter mass lose about 10% of their stellar mass (Smith et al. 2016). As such, tidal stripping of dark matter precedes tidal stripping of stars.

We approximate stellar mass and ISM gas loss via tidal stripping treatment using the "simple" model in Galacticus. This model assumes the stellar mass-loss rate scales with the ratio of tidal force to restoring force in a galaxy at half mass–radius, and is inversely proportional to the dynamical timescale

$$\dot{M}_* = \beta_{\rm tidal}\frac{F_{\rm tidal}}{F_{\rm res}}\frac{1}{T_{\rm dyn}}M_*, \quad (11)$$

Table 1
Summary of the Semianalytic Model Parameters

Notation	Meaning of Parameter	Range of Parameters	Best-fit Value
$z_{\rm reion}$	Reionization suppression redshift	9	9
$v_{\rm filter}$	Reionization suppression velocity	20, 25, 30 km s^{-1}	25 km s^{-1}
$v_{\rm cooling}$	Cooling rate cutoff velocity	15–20 km s^{-1}	19 km s^{-1}
$\dot{\Sigma}_{\rm SF}$	Star formation rate surface density	Extended Schmidt	$e_* = 0.5$, $e_{\rm gas} = 1.09$
…	…	Blitz Rosolowsky	Blitz Rosolowsky $\alpha = 0.92$
…	…	$\alpha = 0.92$	
…	…	Kennicutt Schmidt	
…	…	$e_* = 0.5$, $e_{\rm gas} = 1.09$	
…	…	Krumholz McKee Tumlinson	
…	…	$f = 0.385$, $C = 5$	
$v_{\rm charac}$	Characteristic velocity (disk)	60, 160, 260 km s^{-1}	160 km s^{-1}
$v_{\rm charac}$	Characteristic velocity (sph)	51, 151, 251 km s^{-1}	151 km s^{-1}
$\alpha_{\rm outflow,disk}$	Outflow velocity exponent (disk)	1.7, 2.2, 2.7	
$\alpha_{\rm outflow,sph}$	Outflow velocity exponent (spheroid)	0.3, 0.8, 1.3	
$\beta_{\rm ram}$	Ram pressure stripping efficiency	0.01, 0.1, 1.0	1.00
$\beta_{\rm tidal}$	Tidal stripping efficiency	0.01, 0.1, 1.0	0.01

Note. The first column lists the notation for parameters used in the SAM. The second column explains the meaning of each parameter. The third column lists the range of tested values. The fourth column lists the best-fit values found.

where $\beta_{\rm tidal}$ is the strength of tidal stripping of ISM and stars, $F_{\rm tidal}$ is the tidal force, $F_{\rm res}$ is the restoring force, $T_{\rm dyn}$ is the dynamical time of stars, and M_* is the stellar mass. Note that this model only captures the effects of tidal stripping on the total stellar mass and ignores the effects on the shape of the galaxy's density profile.

Stellar Feedback: We next determine the parameterization of stellar feedback that best produces the observed luminosity–metallicity relation. Stellar feedback from the disk and spheroid components are treated separately, but with the same model, parameterized by a characteristic velocity and exponent. The characteristic velocity defines the scale at which supernovae feedback results in a mass-loading factor (the ratio of the outflow rate to the star formation rate) as one. The outflow rate is then given by

$$\dot{M}_{\rm outflow} = \left(\frac{v_{\rm charac}}{v_{\rm rs}}\right)^{\alpha_{\rm outflow}} \frac{\dot{E}_*}{\epsilon_{\rm cannonical*}}, \quad (12)$$

where $v_{\rm charac}$ (the circular velocity at which the mass outflow rate driven by supernovae equals the star formation rate in the disk/spheroid) at scale radius, $v_{\rm rs}$ is the disk/spheroid circular characteristic velocity at scale radius, and $\alpha_{\rm outflow}$, the disk/spheroid exponent. These are tunable parameters except for $v_{\rm rs}$. $\dot{E}_*$ is the rate of energy input from stellar populations, and $\epsilon_{\rm cannonical*} = 4.517 \times 10^5 ({\rm km\ s^{-1}})^2$ is the total energy input by a canonical stellar population normalized to $1\,M_\odot$ after infinite time. (Note that Galacticus calculates $\epsilon_{\rm cannonical*}$ for a Salpeter IMF and it serves only as a plausible scale.) For a typical low-mass dwarf, the ratio of $v_{\rm charac}/v_{\rm rs}$ would be higher; thus, more mass would escape its potential well, whereas a higher-mass dwarf would have a lower ratio.

The best-fit parameters described above are summarized in Table 1.

3. Results

We initially explore whether there is a set of input parameters for which running Galacticus on a high-resolution *N*-body merger tree will reproduce the luminosities and metallicities of the Milky Way dwarfs.

3.1. Luminosity Function

We begin our exploration of the best-fit Galacticus parameters by determining the combination of $v_{\rm cooling}$ and $v_{\rm filter}$ that best reproduce the observed luminosity function of the Milky Way dwarfs and the simulated luminosity functions from the Mint Justice League (Applebaum et al. 2021) and FIRE II mock observations (Shipp et al. 2022). For Mint Justice League, we use Sandra ($2.4 \times 10^{12}\,M_\odot$) and Elena ($7.5 \times 10^{11}\,M_\odot$) since they are the only simulations run at Mint resolution ($M_V < -5$). They also have virial masses closest to our Milky Way analog ($1.8 \times 10^{12}\,M_\odot$ or $1.2 \times 10^{12}\,M_\odot\,h^{-1}$). We compare our models to three Milky Way analogs (m12f, m12m, m12i) of FIRE II hydrodynamic simulations These simulations resolve halos down to mass scales corresponding to a hosted galaxy luminosity of $M_V < -8$. Masses of m12f, m12m, m12i are $1.7 \times 10^{12}\,M_\odot$, $1.6 \times 10^{12}\,M_\odot$, and $1.2 \times 10^{12}\,M_\odot$, respectively.

While the luminosity functions of the hydrodynamical simulations may undercount the number of ultrafaint dwarfs due to overmerging (Graus et al. 2019), they do not have the completeness issues of the observation sample (Drlica-Wagner et al. 2020).

Figure 2 shows the luminosity function of the satellites in our Milky Way analog modeled by Galacticus with $v_{\rm cooling} = 15$–20 km s^{-1} and $v_{\rm filter} = 20$–30 km s^{-1}. It shows the effect of our choices of $v_{\rm cooling}$ and $v_{\rm filter}$, for $z_{\rm reion} = 9$. The filtering velocity is only allowed to range from 20–30 km s^{-1} (Gnedin & Kravtsov 2006; Bovill & Ricotti 2011). The choice of the range of $v_{\rm cooling}$ and $v_{\rm filter}$ approximates the known physics that suppresses gas accretion and cooling in low-mass halos. In this work, we hold the reionization redshift of the Milky Way constant.

To determine the combinations of $v_{\rm cooling}$ and $v_{\rm filter}$ that produce the best agreement with the known Milky Way satellite population, we compare our models to the observed luminosity function (McConnachie 2012; Drlica-Wagner et al. 2020) and the simulated luminosity function from the two halos

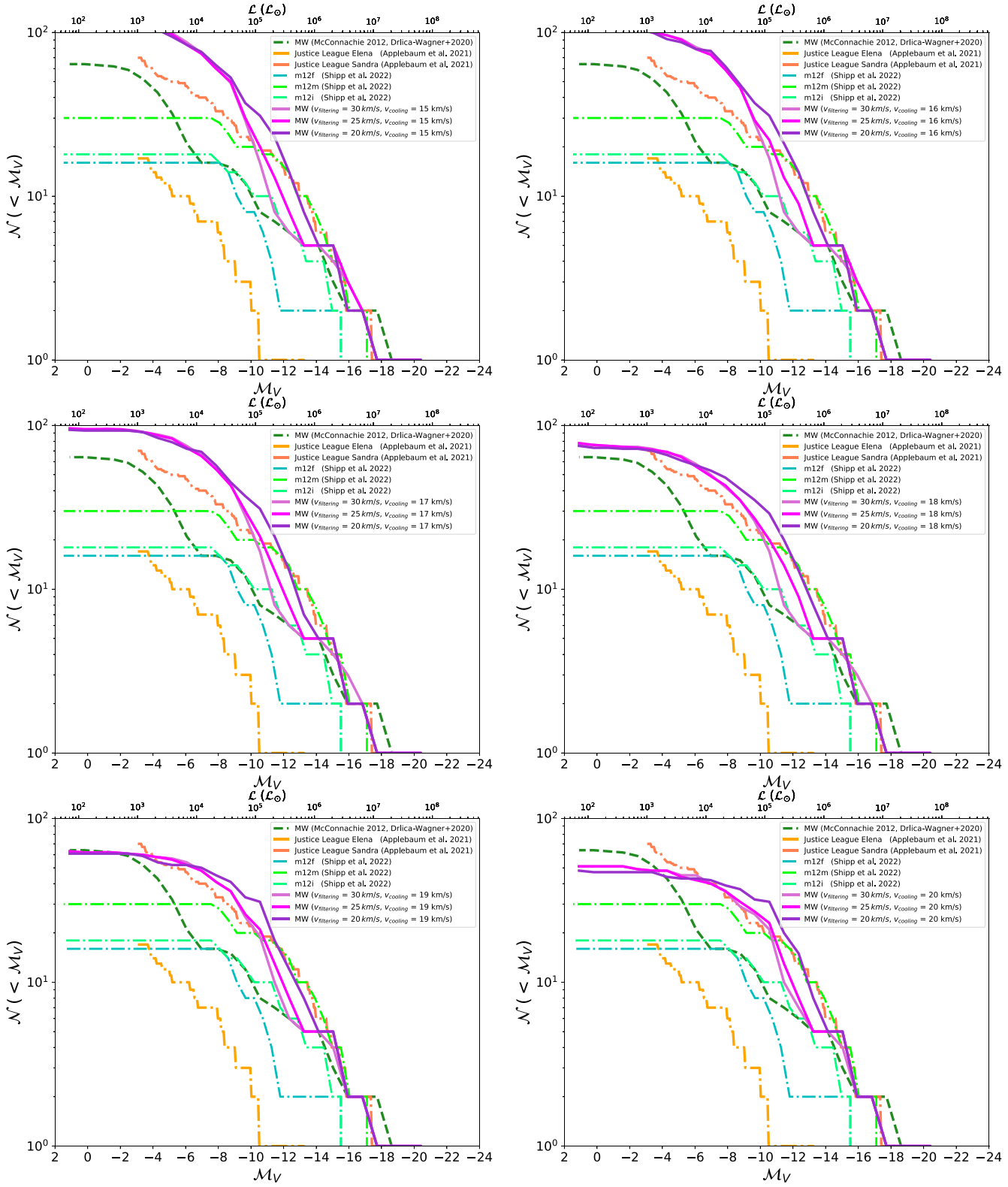

Figure 2. Cumulative luminosity function of the Milky Way dwarf satellite galaxies. M_V denotes the absolute V-band magnitude, and $\mathcal{N}$ denotes the cumulative number of galaxies fainter than M_V. The dark-green dashed line shows the observed data from McConnachie (2012) and Drlica-Wagner et al. (2020). Each figure corresponds to Galacticus runs with cooling rate cutoff velocities from 15–20 km s^{-1}. These predicted luminosity functions correspond to $v_{\rm filter} = 20$, 25, and 30 km s^{-1}, and are then compared to Justice League hydro simulations (shown in orange and coral), and mock observations of FIRE II hydro simulations (in shades of green) along with observations.

in the Mint Justice League (Applebaum et al. 2021) simulations. The latter minimizes the complications due to the incompleteness of the sample of Milky Way satellites, especially at $M_V > -10$ (Willman et al. 2004). Note that we use the updated version of McConnachie (2012) as of 2021 January. Drlica-Wagner et al. (2020) attempted to correct for

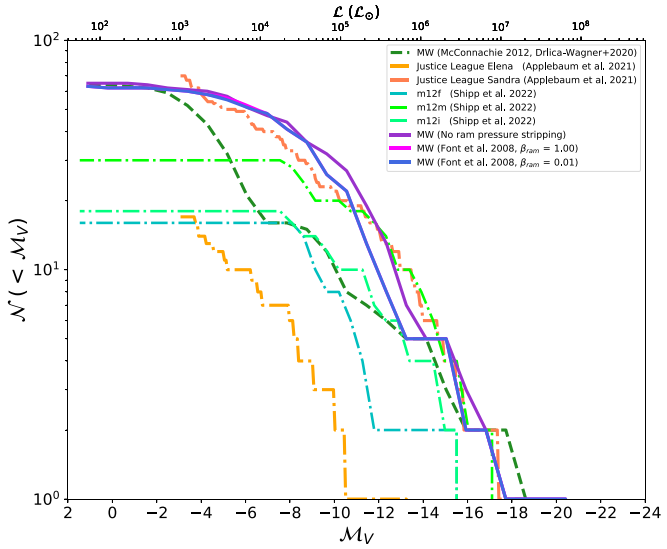

Figure 3. Cumulative luminosity function of the Milky Way satellites computed with ram pressure stripping methods (Font et al. 2008, pink) and $\beta_{\rm ram} = 1.00$ (pink), no ram pressure stripping (purple), and the same method implemented with $\beta_{\rm ram} = 0.01$ (blue). Other colors are the same as in Figure 2.

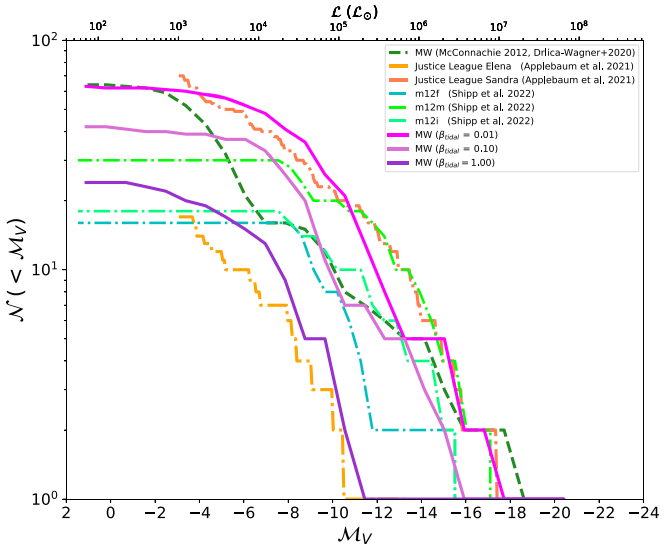

Figure 4. Luminosity function of Milky Way dwarfs for varying tidal stripping efficiencies. Three colors (violet, fuchsia, and purple) indicate tidal stripping efficiencies for stars and ISM gas ($\beta_{\rm tidal} =$ 0.01, 0.1, and 1, respectively). Lower efficiency is in agreement with observations and results of "Mint" resolution Justice League, and FIRE-II hydrodynamic simulations (the colors are the same as in Figure 2).

the survey incompleteness to find the total number of dwarfs in DES and Pan-STARRS1(PS1) surveys. We find that $v_{\rm cooling}$ plays a critical role in producing the correct number of dwarf galaxies fainter than $M_V \geqslant -8$, while $v_{\rm filter}$ primarily affects brighter dwarfs. Our model produces the best fit to the luminosity function of the Milky Way satellites ($M_V < -6$) and Sandra (Applebaum et al. 2021) for $v_{\rm cooling} = 18$–19 km s^{-1} with $v_{\rm filter} = 25$ km s^{-1}.

We note that the observed MW satellites are certainly incomplete below $M_V \sim -10$. For our best-fit model, we match galaxies brighter than $M_V = -6$ and fainter than $M_V = -12$. Note that we slightly overproduce the number of galaxies in the range of $M_V = -12$ and $M_V = -16$ (Figure 2 bottom-left panel, MW—$V_{\rm filter} = 25$ km s^{-1}, $v_{\rm cooling} = 19$ km s^{-1}). In addition, the number of brighter satellites is underpredicted in comparison to observations and hydrodynamic simulations (middle line shown in pink). As the number of bright satellites around a Milky Way mass host is low, this may simply be due to small number statistics.

Notice that there is more than one set of parameters for $v_{\rm cooling}$ and $v_{\rm filter}$ that will produce a reasonable fit to the luminosity function of the observed Milky Way satellites and the Mint Justice League. Specifically, our fit is not improved markedly for $v_{\rm filter} = 25$–30 km s^{-1} and $v_{\rm cooling} \sim 18$–20 km s^{-1}. In this work, we choose our best-fit value for $v_{\rm cooling}$ to approximate the atomic cooling threshold during the epoch of reionization. Our "best-fit" $v_{\rm filter}$ is chosen to be the average of the values used in Ricotti & Gnedin (2005) and Bovill & Ricotti (2011).

In Figure 3 we compare the cumulative luminosity function for the Milky Way satellites computed with the Font et al. (2008) ram pressure stripping model (pink), to that computed in a model with no ram pressure stripping (purple).

We now look at the effect of ram pressure stripping for our best-fit cooling and filtering velocities. We vary the efficiency of the ram pressure stripping through its full range from 0–1. However, the effect of $\beta_{\rm ram} = 0.01$ seems to be the same as $\beta_{\rm ram} = 1.00$, i.e., the efficiency at which gas is stripped upon infall does not have a major effect on the luminosity except in the more-massive dwarfs (see the blue and pink curves of Figure 3). Note that, with the exception of some minor differences at high luminosity ($M_V < -14$), changing the efficiency of the ram pressure stripping does not significantly affect the luminosities of our modeled galaxies. This is expected, as only the most-massive Milky Way dwarfs formed significant amounts of stars after their infall into the Milky Way halo (Rocha et al. 2012).

We now move onto tidal stripping using the "simple" model in Galacticus. Since, in the *N*-body simulation, there is already stripping of the dark matter halos, we do not implement any additional stripping of the dark matter.

The strength of tidal stripping of ISM gas and stars $\beta_{\rm tidal}$ can be varied from 0–1. Unlike ram pressure stripping, which was insensitive to our choice of $\beta_{\rm ram}$, Figure 4 shows the effect on our luminosity function when the efficiency of tidal stripping is varied. While $\beta_{\rm tidal} \sim 0.1$ seems to better match with the observed luminosity function, we select the model that is closest to Mint Justice League to account for the incompleteness of intermediate MW satellites. We reproduce the observed and simulated (hydrodynamic) luminosity functions with $\beta_{\rm tidal} \sim 0.01$. We find a strong and direct inverse relationship between the efficiency of the tidal stripping and the luminosity function of the Milky Way satellites.

Note that the tidal force in the model is calculated at the pericenter of satellite's orbit. Therefore, the actual tidal force will likely be lower than our estimate. This means that $\beta_{\rm tidal} \ll 1$ is reasonable. In addition, models suggests the majority of the dark matter must be stripped before the stars are stripped (Peñarrubia et al. 2008; Smith et al. 2016). Since all of the dwarf galaxies in our simulation exist in *intact* dark matter halos, this is in line with expectations from Peñarrubia et al. (2008) that >90% of the dark matter halo needs to be stripped before the stars are significantly affected. Our model currently includes only a few halos that have been stripped to this level; thus, low efficiency of tidal stripping used here is in agreement with previous work.

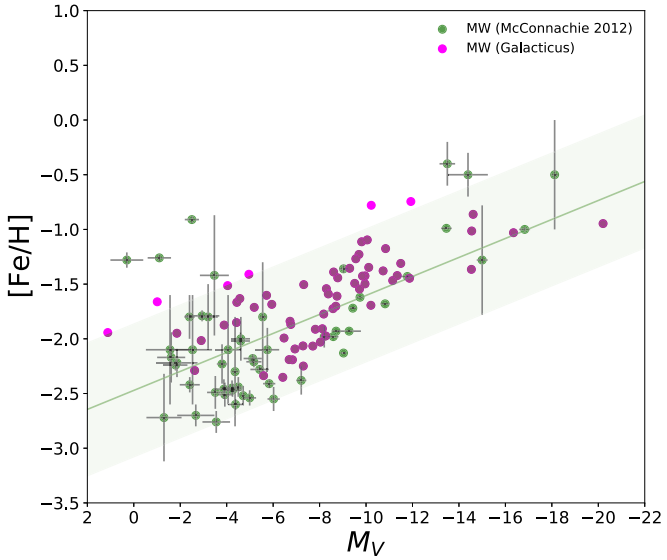

Figure 5. Iron abundance of the dwarf satellite galaxies as a function of absolute *V*-band magnitude. Observed data from McConnachie (2012) are shown in green, and dwarfs modeled with Galacticus are shown in pink. Existing stellar feedback recipes in Galacticus have been calibrated to reproduce the luminosity–metallicity relation.

We also note that our dark-matter-only simulations may suffer from the missing satellite problem (Kauffmann et al. 1993; Klypin et al. 1999; Moore et al. 1999) and lack of modifications to halo concentrations due to baryonic effects. As such, correction models such as in Schneider & Teyssier (2015) may be used to mimic the effects of baryons on the underlying dark matter halos.

3.2. Luminosity–Metallicity Relation

We next determine the combination of stellar feedback parameters that best reproduces the slope of the observed luminosity–metallicity relation (McConnachie 2012). We tune our model for $v_{\rm charac,disk} = 60$, 160, and 260 km s^{-1} for the disk and $v_{\rm charac,sph} = 51$, 151, and 251 km s^{-1} for the spheroidal component. Note that the values used in the standard set of parameters for the baryonic physics of higher-mass galaxies described in Section 2.1 is $v_{\rm charac,disk} = 160$ km s^{-1} and $v_{\rm charac,sph} = 151$ km s^{-1}. Thus, we vary those values by ± 100 km s^{-1}. We find that by tuning the existing stellar feedback recipes in Galacticus, we can reproduce both the trend and scatter in the observed luminosity–metallicity relation (Figure 5). Critically, metallicities of the modeled dwarfs match well with observations down to the ultrafaint dwarfs. The two exponents, $\alpha_{\rm outflow,disk}$ and $\alpha_{\rm outflow,spheroid}$, and the characteristic circular velocity at the scale radius ($v_{\rm charac}$) determine the scaling of the outflow rate of the corresponding disk/spheroid measured at the scale radius of that component. The characteristic velocity determines normalization of the luminosity–metallicity relation, and the exponent of the disk tunes the slope (Figure 6). Higher exponents correspond to steeper slopes and vice versa. In particular, low-mass dwarf galaxies are sensitive to exponents controlling their supernova-driven outflows. The closest match to the slope of the observed luminosity–metallicity relation is obtained for exponents $\alpha_{\rm outflow,disk} = 1.7$ and $\alpha_{\rm outflow,spheroid} = 0.3$.

As seen in Figure 6, while the exponent for the spheroid only marginally affects the slope of the luminosity–metallicity relation, the effect of tuning stellar feedback in the disk component is far greater. We find stellar feedback outflows to be a significant component for tuning the luminosity–metallicity relation. This agrees with Lu et al. (2015), who demonstrated that the metallicity of galaxies provides a constraint on the maximum outflow velocity ($\sim$141 km s^{-1}).

3.3. Properties of the Milky Way Dwarfs

We have determined a set of parameters for Galacticus that reproduce the observed luminosities and metallicities of the Milky Way dwarfs. In this section, we determine if these parameters can reasonably reproduce other properties of the Milky Way dwarfs. Unlike the luminosity function and luminosity–metallicity relation discussed above, we have *not* tuned Galacticus to reproduce any of the dwarf galaxy properties below. All of the observational data in this section comes from the updated table as of 2021 January, originally published in McConnachie (2012).

3.3.1. Half Light Radii

As seen in Figure 7, we are able to match the observed half-light radii for the Milky Way satellites down to $M_V \leqslant -6$. However, our modeled dwarfs have larger half-light radii for fainter, smaller dwarfs, and our modeled half-light radii do not reach below 200 pc. This "floor" in our half-light radii roughly corresponds to the physical softening of our simulations (orange line in Figure 7).

In order to investigate this, we look at the half-light radii as a function of dark matter halo mass (Figure 8). The vertical lines in Figure 8 show the dark matter halo masses for various numbers of particles per halo. Note that halos whose half-light radii are below the "floor" corresponding to the physical softening of our simulation all have >1000 particles. As Galacticus calculates the $r_{\rm hl}$ of the halos by allowing the disk and spheroidal components to evolve within the gravitational potential of a dark matter profile, the determination of $r_{\rm hl}$ relies on a robust determination of the dark matter profile. The underlying NFW profile is set from scale radii of the simulation, where concentrations are calculated using the model by Gao et al. (2008). The equilibrium radii for the disk and the spheroid components are described by the NFW profile, and half-light radii are calculated in the SDSS$_g$ luminosity band. While the global properties of halos with $N < 1000$ particles are relatively certain (Trenti et al. 2010; Benson 2017b), the details of their dark matter profiles are not robust. For example, Mansfield & Avestruz (2021) showed that convergence in measurements of half-mass radii of halos from *N*-body simulations requires >4000 particles.

As the low-mass halos that host the faintest dwarfs in our model have $N < 500$ particles, the uncertainties in the determination of their dark matter profile coupled with the physical gravitational softening used in the simulation produces a "floor" of $\sim$200 pc. Similar effects of resolution are seen in the half-light radii of Mint Justice League simulations by Applebaum et al. (2021).

3.3.2. Velocity Dispersion

We next look at the velocity dispersions of our modeled dwarfs at half-stellar mass radii compared to observations of McConnachie (2012; updated as of 2021 January). Note that Galacticus calculates the velocity dispersion of each satellite

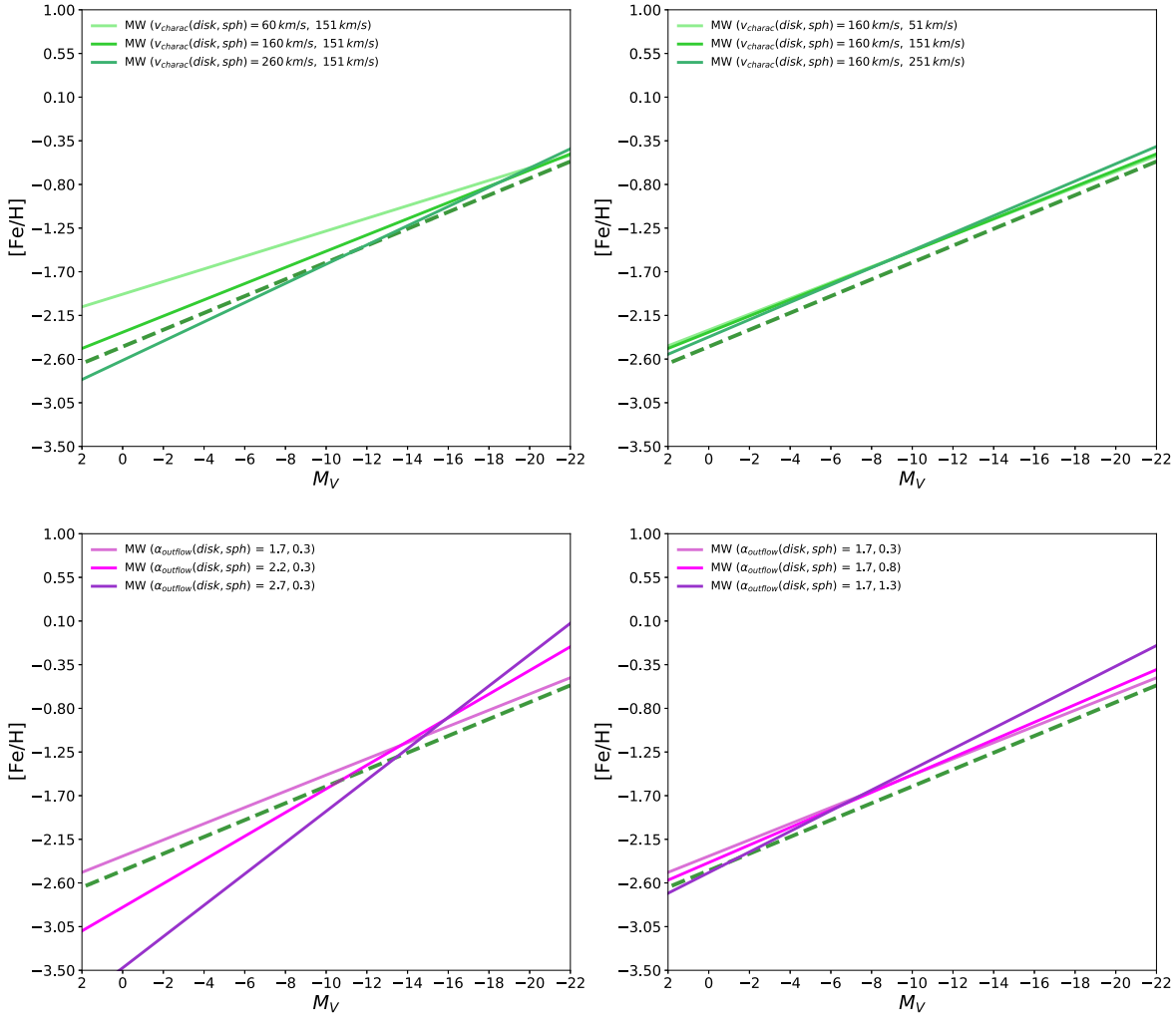

Figure 6. Modeled luminosity–metallicity relations for various characteristic velocities and exponents of stellar outflows. The top-left and -right panels show the effect of the characteristic velocity for the disk and spheroid components, respectively. The bottom-left and -right panels show the effect of exponents on disk and spheroid components. Note that this relation is sensitive to both characteristic velocity (normalization) and exponents of the disk component (slope). The green dashed line shows the best-fit line for the observed luminosity–metallicity relation of McConnachie (2012).

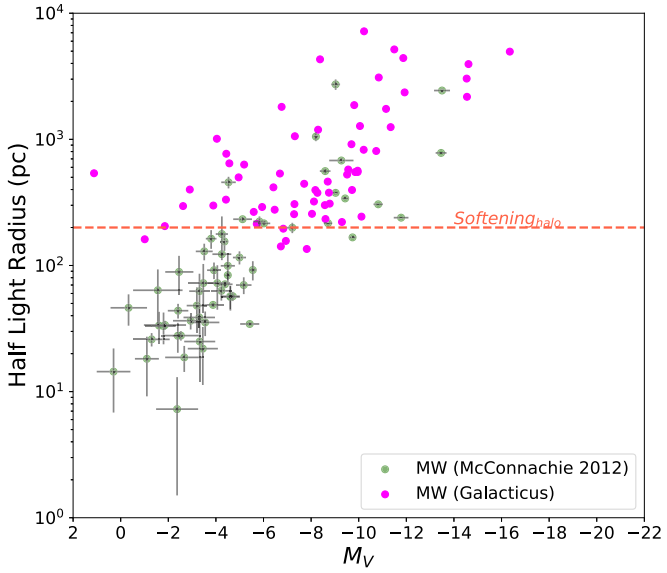

Figure 7. Half-light radii of the dwarf satellite galaxies as a function of absolute *V*-band magnitude. Observed data from McConnachie (2012) are colored in green, and simulated data are colored in pink. The orange dashed line shows the softening of the halo at 200 pc in the *N*-body simulation.

galaxy at its half mass–radius. As seen in Figure 9, the stellar velocity dispersions of our predicted dwarfs agree well with observations. However, note that velocity dispersions of galaxies below $M_V \sim -8$ may be affected by the floor in half-light radii discussed above.

3.3.3. Mass-to-light Ratios

Given that we are able to reasonably reproduce the half-light radii and velocity dispersions of the Milky Way dwarfs, we can estimate the mass-to-light ratios of the modeled Milky Way satellites using the Equation (2) in Wolf et al. (2010). While Galacticus does not calculate mass-to-light ratios directly, we use stellar velocity dispersions and half-light radii to calculate mass-to-light ratios. Our modeled mass-to-light ratios are in good agreement with values derived from observations (Figure 10). Critically, we are able to produce the dark matter domination of the ultrafaints dwarfs (Simon 2019). We quantify the offset in observational and simulation data by using two regression lines (see Figure 10). We find an rms error of 0.84 in log scale.

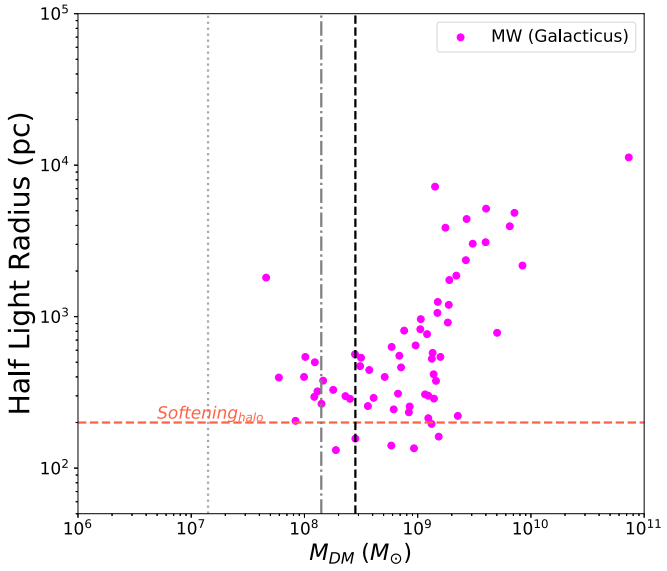

Figure 8. Half-light radii of the dwarf satellite galaxies as a function of dark matter halo mass. Here we show the dark matter mass of halos with 100 (light gray dotted), 1000 (dotted dashed line in dark gray), and 2000 (dashed line in black) particles. The orange dashed line shows the softening of the halo at 200 pc in the *N*-body simulation. Note that most halos need ∼1000 dark matter particles in order to form luminous galaxies.

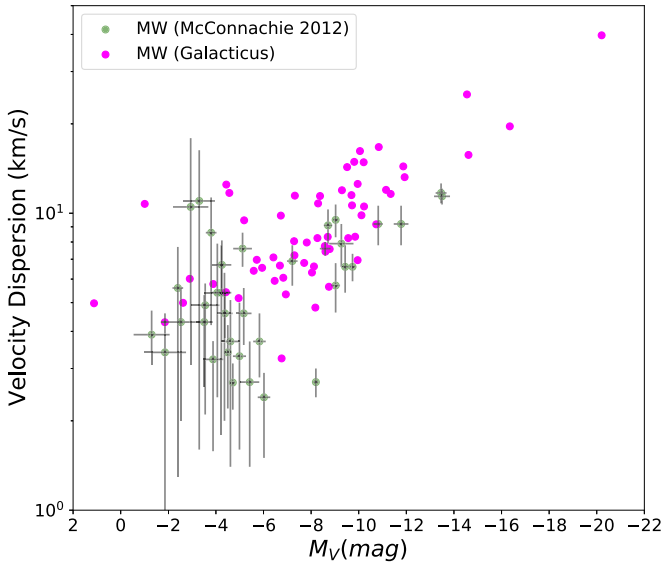

Figure 9. Velocity dispersion of the modeled and observed dwarf satellites as a function of absolute *V*-band magnitude. Observed data from McConnachie (2012) are colored in green, and simulated data are colored in pink. Our model agrees well with observations without additional tuning.

3.4. Star Formation Histories

We have shown that by constraining Galacticus to reproduce the luminosities and metallicities of both the classical and ultrafaint dwarfs, we are able to successfully reproduce a wide range of observed Milky Way dwarf properties at $z = 0$. As a final test, we determine whether we are able to reproduce SFHs that match those derived from observations (Weisz et al. 2014, 2015).

We begin by looking at the cumulative SFHs of the Milky Way dwarfs (Figure 11). Each curve is color-coded by the absolute *V*-band magnitude of a particular halo at $z = 0$.

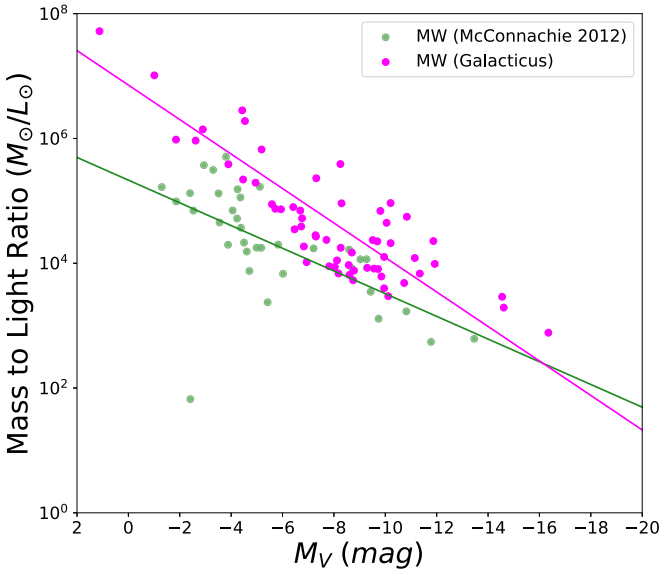

Figure 10. Mass-to-light ratios of the Milky Way satellites as a function of the velocity dispersion along the line of sight. Mass to light is calculated using the half mass with velocity dispersion and half-light radii as described in Wolf et al. (2010). We compare the modeled dwarfs (pink) to observed data from McConnachie (2012; green). Green and pink lines show the linear regression lines for the observed and modeled dwarfs, respectively. Mass-to-light ratios of the Milky Way satellites are in agreement down to the ultrafaints, though our mass-to-light ratios are a bit higher than observed values.

As expected (Brown et al. 2014; Sacchi et al. 2021), fainter dwarfs ($M_V \geqslant -6$) accumulated the majority of their current stellar mass more than 11 ± 1 Gyr ago. In contrast, the more luminous model dwarfs at $z = 0$ form their stars over longer periods of time, including some systems that are still star-forming today. We note that some of the modeled cumulative SFHs plateau around 0.1, 0.3, and 0.6, which is similar to the observed SFHs of Weisz et al. (2014) shown in Figure 11. Note that all observed SFHs of dwarfs plotted in the middle and right panels of Figure 11 have similar luminosities. All of these dwarfs, other than Sculptor, quench later. However, our modeled dwarfs quench early, at ∼11–12 Gyr. Cumulative SFHs derived from Galacticus are consistent with the results of Mint Justice League simulations (Figure 11 of Applebaum et al. 2021).

The faintest modeled dwarfs all have their star formation cut off at about the same time. This is expected as the faintest observed Milky Way satellites are the fossils of the first galaxies (Bovill & Ricotti 2011; Brown et al. 2012). The larger range in the lookback time of the truncation of star formation for the more luminous dwarfs is consistent with their star formation being shut off upon accretion into the Milky Way halo.

We next look at quenching times of these dwarf galaxies, specifically, the time for a galaxy to gain 90% its current stellar mass (τ_{90}) and for a galaxy to gain 50% its current stellar mass (τ_{50}). We reproduce the τ_{90} versus τ_{50} plot from Figure 3 of Weisz et al. (2019) to compare the overall distribution of SFHs of the modeled versus observed dwarfs. Interestingly, we are unable to reproduce the lack of galaxies inside the blue dotted rectangle in Figure 12, which is a feature Weisz et al. (2019) identified in the Milky Way dwarfs; however, no such feature is seen for the M31 dwarfs, in agreement with Figure 12.

Despite our overall good agreement, there are interesting distinctions between the modeled and observed τ_{90}–τ_{50}.

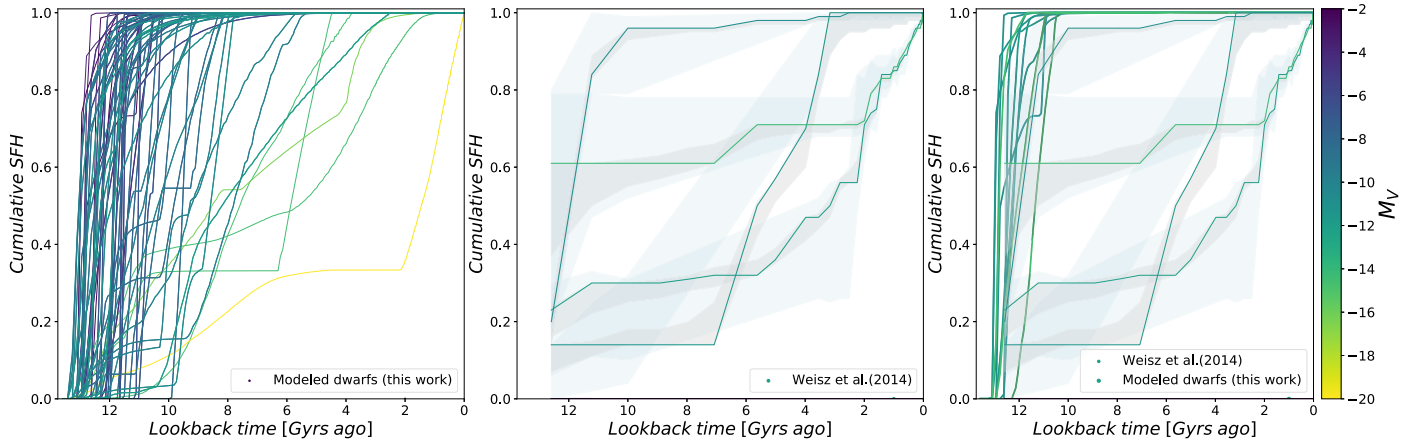

Figure 11. Cumulative star formation histories (SFHs) of the Milky Way satellites colored by absolute V-band magnitude. The left panel shows the SFHs modeled with Galacticus, and the middle panel shows observed SFHs for Leo A, Sagittarius, Sex A, and Sculptor by Weisz et al. (2014). Note that we plot only the SFHs of the MW satellites from a list of combined SFHs of dwarfs of the Local Group with multiple fields in Weisz et al. (2014). While not intentional, the brightnesses of this observed sample of galaxies are similar. The shaded regions in the middle and right panels show the region between the 16th and 84th percentiles in SFH uncertainties (gray for random uncertainty, and blue for total uncertainty). In the right panel, we plot SFH of models that have similar brightnesses to dwarfs of Weisz et al. (2014; models are shown in thick lines, while observations are shown in thin lines). While most observed dwarfs quench later except Sculptor, our models quench early ($\sim$11 Gyr ago). Note that Weisz et al. (2014) used isochrones older than the age of the universe, and set the cumulative SFHs to 0 at $\log(t) = 10.15$ Gyr. We have not made any correction to account for this in the modeled SFHs. Our cumulative SFHs are somewhat consistent with these results and the SFHs of the ultrafaints (Brown et al. 2014). However, since our models exclude H_2 cooling, we preclude comparison of modeled ultrafaints to dwarfs of Brown et al. (2014).

Figure 12 shows that our τ_{90} values match well with quenching times for Milky Way satellites by Weisz et al. (2019). In Figure 13, we compare the τ_{90} distributions of Weisz et al. (2015) for the Milky Way, M31, and the Local Group as whole. A two-sample Kolmogorov–Smirnov test on the observed distributions with models results in a $p = 0.28$ for the Milky Way, $p = 0.98$ for the Local Group, and $p = 0.66$ for M31 with $\alpha = 0.05$, respectively. Since all p-values are not less than the corresponding α value, the modeled distributions come from the observed distributions of τ_{90} that are not very different. Yet, there may be disagreement between the modeled and observed SFHs or inherent scatter in τ_{90} between halos. However a further exploration of this is beyond the scope of this work.

In contrast, we find a systematic delay of τ_{50} in our model of about 500 Myr for the ultrafaint dwarfs. This delay may be due to the lack of molecular hydrogen cooling in our models, delaying the start of star formation until a halo has $v_{\rm vir} > v_{\rm cooling}$, with $v_{\rm cooling}$ chosen to approximate the atomic cooling threshold. While delaying star formation until after the atomic cooling limit does not create the same systematic effect for τ_{90}, it will take the halos longer to form 50% of their $z = 0$ stellar populations. We also find the most luminous satellites in our model to have $\tau_{50} < 2$ Gyr. This is a peculiar case since most recent star formation in the Milky Way satellite system took place over 3–6 Gyr based on Weisz et al. (2019).

4. Discussion

As discussed in Section 1, the well-studied Milky Way satellites are an ideal data set for constraining parameters of Galacticus to best model dwarf galaxies. The initial goal of this study was to build a viable model of the classical dwarfs in the Milky Way and explore predictions for their SFHs with the standard implementation of Galacticus. However, in addition to successfully modeling the properties of the classical Milky Way satellites, we are also able to match the properties of the more luminous ultrafaint dwarfs. Reproducing the stellar properties of the Milky Way satellites, including the ultrafaint fossil galaxies, was unexpected due to the stochastic star formation processes that govern the evolution of the lowest-mass galaxies (Guo et al. 2016). In addition to the properties at $z = 0$, we also reproduce the SFHs and quenching times (τ_{90} versus τ_{50}) of the Local Group dwarfs.

Despite the success of Galacticus in modeling the dwarfs, the match between the $z = 0$ properties and SFHs for the classical and brightest ultrafaints breaks down for the dwarfs below $M_V \sim -6$). Dwarf galaxy halos modeled with Galacticus cool via atomic processes. As discussed in Section 2.1.1, we choose the minimum $v_{\rm vir}$ to approximate the atomic cooling cutoff during reionization. The lowest-mass dwarfs ($M < 10^8\,M_\odot$) initially cooled via the rotational and vibrational transitions of H_2 (Bromm et al. 2009). The lack of H_2 cooling in our model delays the start of star formation in all of our dwarfs. Since the majority of stars in the more luminous dwarfs ($M_V > -8$) formed when their host halos were above the atomic cooling threshold, we are able to model their properties and SFHs. In contrast, as the luminosity, and halo mass (Santos-Santos et al. 2022), of the faintest dwarfs decreases, the fraction of the stars formed with $v_{\rm vir} < v_{\rm cooling}$ increases. Since our model does not currently account for gas cooling via H_2, we are less able to reproduce the properties and SFHs of the latter group. In addition, a subset of the faintest dwarfs never reaches $v_{\rm vir} > v_{\rm cooling}$. As a result, they remain completely dark in our model, an effect seen by the turnover of the modeled luminosity function at $M_V > -4$. The question on whether star formation in halos with masses $<10^8\,M_\odot$ at reionization (below the atomic cooling limit) is required to reproduce the observed properties of UFDs is still an open question. A robust test of what is the minimum halo mass hosting luminous galaxies has been proposed in Kang & Ricotti (2019) and Ricotti et al. (2022) and relies on detecting ("ghostly") stellar halos in isolated dwarf galaxies in the Local Group (e.g., Leo A, WLM, IC 1613, NGC 6822). The first results using this new method seem to indicate that halos with masses as low as $10^7\,M_\odot$ at $z \sim 7$ should be luminous. This is also in agreement with results from DES (Nadler et al. 2020) using halo-matching (Behroozi

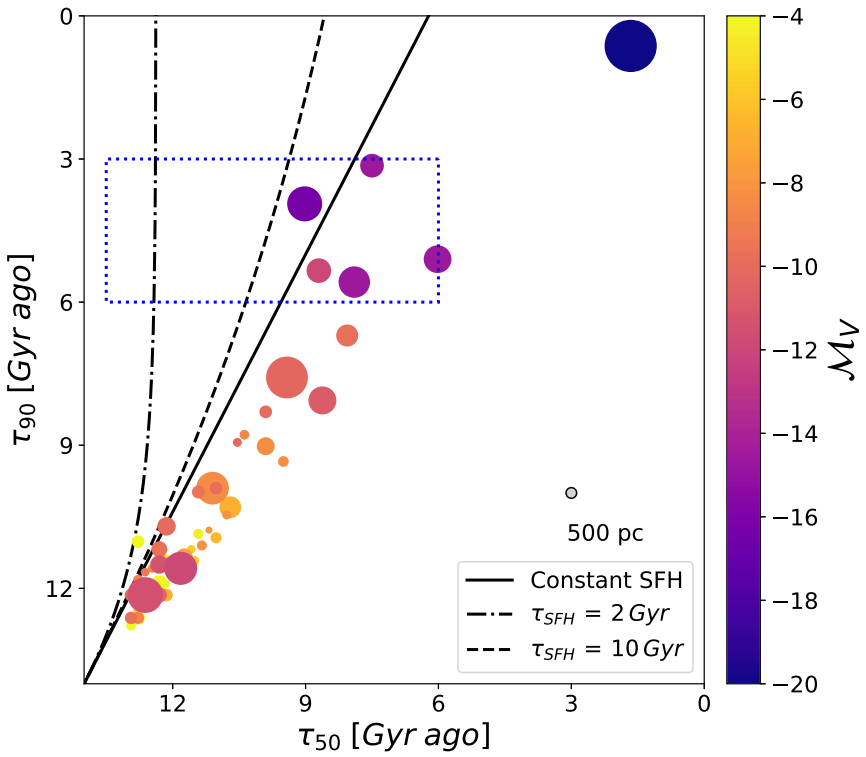

Figure 12. Lookback time at which 90% of the stellar mass formed (τ_{90}) vs. the lookback time at which 50% of the stellar mass formed (τ_{50}). Each point is colored by its absolute V-band magnitude at $z = 0$ and sized relative to their half-light radii in parsecs. The gray dot shows a point with half-light radius of 500 pc. The solid line shows constant SFH. The two dashed lines correspond to exponentially declining SFH (e.g., SFH(t) = $t_0 \cdot e^{-t/2\ \mathrm{Gyr}}$ and SFH(t) = $t_0 \cdot e^{-t/10\ \mathrm{Gyr}}$, respectively, where t_0 is a constant. Compare this plot to Figure 3 in Weisz et al. (2019). Weisz et al. (2019) used the rectangle shown in blue to show the region within which there are no Milky Way satellites, in contrast to the M31 system.

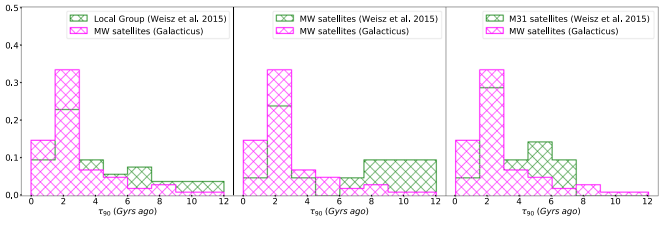

Figure 13. Normalized distribution of τ_{90} in gigayears. Two curves show the predicted values from observations of Weisz et al. (2015; green) and models (pink), respectively. Left panel: comparison of our model to the Local Group dwarfs. Middle panel: comparison of our model to Milky Way dwarfs. Right panel: comparison of our model to M31 dwarfs.

et al. 2019). The inclusion of models of H_2 into Galacticus, and how it effects our modeling of the faintest dwarfs, will be a subject of parallel work.

Several previous studies of dwarf galaxies have been made using SAMs, most of which have found it challenging to reproduce a broad range of dwarf galaxy properties without significant modification to the SAM (e.g., Li et al. 2010; Macciò et al. 2010; Font et al. 2011; Lu et al. 2017; Starkenburg et al. 2013). For example, Lu et al. (2017) found that their SAM could not simultaneously produce a good match to the dwarf galaxy mass function and mass–metallicity relation without the introduction of a preventative feedback model that reduced the fraction of baryons accreting into a halo as a function of its mass and redshift of that halo. Note that Lu et al. (2017) use a relatively simple treatment of subhalos: their model removes circumgalactic medium (CGM) gas from a halo and transfers it to the parent halo as soon as a halo becomes a subhalo. While Galacticus does stop accreting gas onto subhalos, it retains the remaining CGM gas that will continue to cool and supply gas to the subhalo, removing it only gradually via ram pressure stripping, etc. The study by Pandya et al. (2020) found that their SAM predicted gas accretion rates orders of magnitudes higher than those found in the FIRE II simulations (Hopkins et al. 2014, 2018), and were driven to allow stellar feedback to heat gas surrounding halos and thereby preventing it from accreting at such high rates. They also emphasized the possibility of obtaining the same final stellar/ISM mass with different combinations of outflows (e.g., high inflow + high outflow, low inflow + low outflow). Thus, they highlighted the importance of comparing the gas accretion, and outflow rates between models/simulations and observations rather than just bulk integrated properties. Note that their study focused on relatively isolated central dwarfs not satellites of MW analogs. While we have not explored gas accretion rates in this paper, we *have* examined the luminosity function and mass–metallicity relation—essentially the diagnostics used by Lu et al. (2017). Interestingly, we do not find the need for any preventative feedback to simultaneously match both of these quantities.

The reasons for this lack of need for preventative feedback are not immediately clear. While the physics ingredients of the Galacticus SAM are fundamentally very similar to the SAMs of both Lu et al. (2017) and Pandya et al. (2020), there are differences in the details of the physics models. Additionally, there are differences in the numerical implementations of models (e.g., Galacticus uses an adaptive time step ODE solver, while the SAMs of Lu et al. 2017 and Pandya et al. 2020 use fixed steps, often with each physical process applied in

succession, rather than simultaneously). Identifying the primary cause of the lack of need of preventative feedback in Galacticus is a key question, but one that requires an extensive study that is beyond the scope of the present work. Fortunately, the flexible, modular nature of Galacticus allows for the possibility of constructing models that mimic the SAMs of Lu et al. (2017) and Pandya et al. (2020)—this will allow us to explore in detail which physical or numerical choices lead to these different conclusions. We intend to undertake such a detailed study in a follow-up work.

5. Summary and Conclusions

In this work, we have modeled the Milky Way satellites using the semianalytic model Galacticus (Benson 2012) run on merger trees from a high-resolution *N*-body simulation of a Milky Way analog. Using available astrophysical priors, we tune the gas cooling in halos, star formation, and feedback recipes to reproduce the observed luminosity function and the luminosity–metallicity relation of the Milky Way satellites (McConnachie 2012; Drlica-Wagner et al. 2020) and the simulated luminosity functions from the Mint Justice League (Applebaum et al. 2021), and mock observations of FIRE-II (Shipp et al. 2022).

Our conclusions are as follows.

1. We reproduce the luminosities and metallicities of the Milky Way satellites down to $M_V \sim -6$. In addition, despite the lack of H_2 cooling in our current model, we successfully model the properties of the most luminous of the ultrafaint fossil dwarfs.
2. When our model is tuned to reproduce the observed luminosity function and luminosity–metallicity relation, we are able to independently reproduce several $z = 0$ properties of the Milky Way dwarfs, including half-light radii, velocity dispersions, and mass-to-light ratios without any additional tuning of the physics.
3. In addition to reproducing the observed $z = 0$ properties of Milky Way dwarfs with $M_V < -6$, our work produces SFHs that are consistent with observations (Weisz et al. 2014, 2019). As with the additional $z = 0$ dwarf properties, this is done without any additional tuning of the baryonic physics. We also find that the quenching timescale of our modeled dwarfs is in reasonable agreement with that for the M31 dwarfs.

This work shows the ability of Galacticus to reproduce the $z = 0$ properties and SFHs of dwarf galaxies down to the luminous ultrafaints, providing a new tool for investigating the astrophysics of star formation and feedback in the lowest-mass systems.

We would like to thank the anonymous referee for providing thoughtful comments that improved this work. The authors acknowledge the University of Maryland supercomputing resources (http://hpcc.umd.edu) made available for conducting the research reported in this paper. We thank Ferah Munshi, Charlotte Christensen, Alyson Brooks of Mint Justice League collaboration and Nondh Panithanpaisal, Nora Shipp, and Robyn Sanderson of FIRE-II collaboration for providing access to their respective luminosity functions. S.W. thanks Alessa Ibrahim Wiggins and Natalie Myers for proof reads. M.S.B. and S.W. thank Minerva for many contributing conversations and encouragement.

ORCID iDs

Sachi Weerasooriya https://orcid.org/0000-0001-9485-6536
Mia Sauda Bovill https://orcid.org/0000-0003-4037-5360
Andrew Benson https://orcid.org/0000-0001-5501-6008
Massimo Ricotti https://orcid.org/0000-0003-4223-7324

References

Abbott, T. M. C., Abdalla, F. B., Alarcon, A., et al. 2018, PhRvD, 98, 043526
Aguado, D. S., Ahumada, R., Almeida, A., et al. 2019, ApJS, 240, 23
Albareti, F. D., Allende Prieto, C., Almeida, A., et al. 2017, ApJS, 233, 25
Alvarez, M. A., Busha, M., Abel, T., & Wechsler, R. H. 2009, ApJL, 703, L167
Applebaum, E., Brooks, A. M., Christensen, C. R., et al. 2021, ApJ, 906, 96
Aubert, D., Deparis, N., Ocvirk, P., et al. 2018, ApJL, 856, L22
Baldry, I. K., Driver, S. P., Loveday, J., et al. 2012, MNRAS, 421, 621
Behroozi, P., Wechsler, R. H., Hearin, A. P., & Conroy, C. 2019, MNRAS, 488, 3143
Behroozi, P. S., Wechsler, R. H., & Wu, H.-Y. 2013a, ApJ, 762, 109
Behroozi, P. S., Wechsler, R. H., Wu, H.-Y., et al. 2013b, ApJ, 763, 18
Benítez-Llambay, A., Navarro, J. F., Frenk, C. S., et al. 2017, MNRAS, 465, 3913
Benson, A. J. 2012, NewA, 17, 175
Benson, A. J. 2017a, MNRAS, 471, 2871
Benson, A. J. 2017b, MNRAS, 467, 3454
Benson, A. J., & Bower, R. 2010, MNRAS, 405, 1573
Benson, A. J., Lacey, C. G., Baugh, C. M., Cole, S., & Frenk, C. S. 2002, MNRAS, 333, 156
Birnboim, Y., & Dekel, A. 2003, MNRAS, 345, 349
Blanc, G. A., Lu, Y., Benson, A., Katsianis, A., & Barraza, M. 2019, ApJ, 877, 6
Blitz, L., & Rosolowsky, E. 2006, ApJ, 650, 933
Bose, S., Deason, A. J., Belokurov, V., & Frenk, C. S. 2020, MNRAS, 495, 743
Bovill, M. S., & Ricotti, M. 2009, ApJ, 693, 1859
Bovill, M. S., & Ricotti, M. 2011, ApJ, 741, 17
Bower, R. G., Vernon, I., Goldstein, M., et al. 2010, MNRAS, 407, 2017
Bromm, V., Yoshida, N., Hernquist, L., & McKee, C. F. 2009, Natur, 459, 49
Brown, T. M., Tumlinson, J., Geha, M., et al. 2012, ApJL, 753, L21
Brown, T. M., Tumlinson, J., Geha, M., et al. 2014, ApJ, 796, 91
Bryan, G. L., & Norman, M. L. 1998, ApJ, 495, 80
Bullock, J. S., & Johnston, K. V. 2005, ApJ, 635, 931
Bullock, J. S., Kravtsov, A. V., & Weinberg, D. H. 2000, ApJ, 539, 517
Busha, M. T., Alvarez, M. A., Wechsler, R. H., Abel, T., & Strigari, L. E. 2010, ApJ, 710, 408
Chen, L.-H., Magg, M., Hartwig, T., et al. 2022, MNRAS, 513, 934
Cole, S., Lacey, C. G., Baugh, C. M., & Frenk, C. S. 2000, MNRAS, 319, 168
Crnojevic, D. 2020, AAS Meeting, 235, 207.13
Dekel, A., & Silk, J. 1986, ApJ, 303, 39
Drlica-Wagner, A., Bechtol, K., Mau, S., et al. 2020, ApJ, 893, 47
Fardal, M. A., Katz, N., Gardner, J. P., et al. 2001, ApJ, 562, 605
Ferguson, H. C., & Binggeli, B. 1994, A&ARv, 6, 67
Fitts, A., Boylan-Kolchin, M., Elbert, O. D., et al. 2017, MNRAS, 471, 3547
Font, A. S., Benson, A. J., Bower, R. G., et al. 2011, MNRAS, 417, 1260
Font, A. S., Bower, R. G., McCarthy, I. G., et al. 2008, MNRAS, 389, 1619
Gao, L., Navarro, J. F., Cole, S., et al. 2008, MNRAS, 387, 536
Geha, M., Wechsler, R. H., Mao, Y.-Y., et al. 2017, ApJ, 847, 4
Gnedin, N. Y. 2000, ApJ, 542, 535
Gnedin, N. Y., & Kravtsov, A. V. 2006, ApJ, 645, 1054
Graus, A. S., Bullock, J. S., Kelley, T., et al. 2019, MNRAS, 488, 4585
Gunawardhana, M. L. P., Hopkins, A. M., Bland-Hawthorn, J., et al. 2013, MNRAS, 433, 2764
Guo, Y., Rafelski, M., Faber, S. M., et al. 2016, ApJ, 833, 37
Hahn, O., & Abel, T. 2011, MNRAS, 415, 2101
Hatton, S., Devriendt, J. E. G., Ninin, S., et al. 2003, MNRAS, 343, 75
Helly, J. C., Cole, S., Frenk, C. S., et al. 2003, MNRAS, 338, 903
Henriques, B. M. B., Thomas, P. A., Oliver, S., & Roseboom, I. 2009, MNRAS, 396, 535
Hopkins, P. F., Kereš, D., Oñorbe, J., et al. 2014, MNRAS, 445, 581
Hopkins, P. F., Wetzel, A., Kereš, D., et al. 2018, MNRAS, 480, 800
Iliev, I. T., Moore, B., Gottlöber, S., et al. 2011, MNRAS, 413, 2093
Jackson, R. A., Kaviraj, S., Martin, G., et al. 2021, MNRAS, 502, 1785
Jiang, F., Dekel, A., Freundlich, J., et al. 2021, MNRAS, 502, 621
Kang, H. D., & Ricotti, M. 2019, MNRAS, 488, 2673

Kauffmann, G., Colberg, J. M., Diaferio, A., & White, S. D. M. 1999, MNRAS, 303, 188
Kauffmann, G., White, S. D. M., & Guiderdoni, B. 1993, MNRAS, 264, 201
Kennicutt, R. C., Jr. 1998, ApJ, 498, 541
Kereš, D., Katz, N., Davé, R., Fardal, M., & Weinberg, D. H. 2009, MNRAS, 396, 2332
Kereš, D., Katz, N., Weinberg, D. H., & Davé, R. 2005, MNRAS, 363, 2
Klypin, A., Kravtsov, A. V., Valenzuela, O., & Prada, F. 1999, ApJ, 522, 82
Knollmann, S. R., & Knebe, A. 2009, ApJS, 182, 608
Kormendy, J., & Ho, L. C. 2013, ARA&A, 51, 511
Leauthaud, A., Tinker, J., Bundy, K., et al. 2012, ApJ, 744, 159
Li, T. Y., Alvarez, M. A., Wechsler, R. H., & Abel, T. 2014, ApJ, 785, 134
Li, Y.-S., De Lucia, G., & Helmi, A. 2010, MNRAS, 401, 2036
Lu, Y., Benson, A., Wetzel, A., et al. 2017, ApJ, 846, 66
Lu, Y., Blanc, G. A., & Benson, A. 2015, ApJ, 808, 129
Macciò, A. V., Frings, J., Buck, T., et al. 2017, MNRAS, 472, 2356
Macciò, A. V., Kang, X., Fontanot, F., et al. 2010, MNRAS, 402, 1995
Mansfield, P., & Avestruz, C. 2021, MNRAS, 500, 3309
Mao, Y.-Y., Geha, M., Wechsler, R. H., et al. 2021, ApJ, 907, 85
Martin, A. M., Papastergis, E., Giovanelli, R., et al. 2010, ApJ, 723, 1359
Martin, N. F., Ibata, R. A., Lewis, G. F., et al. 2016, ApJ, 833, 167
McConnachie, A. W. 2012, AJ, 144, 4
Moffett, A. J., Lange, R., Driver, S. P., et al. 2016, MNRAS, 462, 4336
Monaco, P., Fontanot, F., & Taffoni, G. 2007, MNRAS, 375, 1189
Montero-Dorta, A. D., & Prada, F. 2009, MNRAS, 399, 1106
Moore, B., Ghigna, S., Governato, F., et al. 1999, ApJL, 524, L19
More, S., van den Bosch, F. C., Cacciato, M., et al. 2009, MNRAS, 392, 801
Munshi, F., Brooks, A. M., Applebaum, E., et al. 2021, ApJ, 923, 35
Muzzin, A., Marchesini, D., Stefanon, M., et al. 2013, ApJ, 777, 18
Nadler, E. O., Wechsler, R. H., Bechtol, K., et al. 2020, ApJ, 893, 48
Ocvirk, P., Aubert, D., Chardin, J., et al. 2013, ApJ, 777, 51
Okamoto, T., Frenk, C. S., Jenkins, A., & Theuns, T. 2010, MNRAS, 406, 208
Pandya, V., Somerville, R. S., Anglés-Alcázar, D., et al. 2020, ApJ, 905, 4
Peñarrubia, J., Navarro, J. F., & McConnachie, A. W. 2008, ApJ, 673, 226
Polisensky, E., & Ricotti, M. 2011, PhRvD, 83, 043506
Press, W. H., & Schechter, P. 1974, ApJ, 187, 425
Ricotti, M., & Gnedin, N. Y. 2005, ApJ, 629, 259
Ricotti, M., Parry, O. H., & Gnedin, N. Y. 2016, ApJ, 831, 204
Ricotti, M., Polisensky, E., & Cleland, E. 2022, MNRAS, 515, 302
Rocha, M., Peter, A. H. G., & Bullock, J. 2012, MNRAS, 425, 231
Sacchi, E., Richstein, H., Kallivayalil, N., et al. 2021, ApJL, 920, L19
Santos-Santos, I. M. E., Sales, L. V., Fattahi, A., & Navarro, J. F. 2022, MNRAS, 515, 3685
Sawala, T., Frenk, C. S., Fattahi, A., et al. 2016, MNRAS, 456, 85
Schneider, A., & Teyssier, R. 2015, JCAP, 2015, 049
Shen, S., Mo, H. J., White, S. D. M., et al. 2003, MNRAS, 343, 978
Shi, Y., Helou, G., Yan, L., et al. 2011, ApJ, 733, 87
Shipp, N., Panithanpaisal, N., Necib, L., et al. 2022, arXiv:2208.02255
Simon, J. D. 2019, ARA&A, 57, 375
Smith, R., Choi, H., Lee, J., et al. 2016, ApJ, 833, 109
Smith, R., Sánchez-Janssen, R., Fellhauer, M., et al. 2013, MNRAS, 429, 1066
Sobral, D., Smail, I., Best, P. N., et al. 2013, MNRAS, 428, 1128
Somerville, R. S., & Davé, R. 2015, ARA&A, 53, 51
Somerville, R. S., & Primack, J. R. 1999, MNRAS, 310, 1087
Sorgho, A., Foster, T., Carignan, C., & Chemin, L. 2019, MNRAS, 486, 504
Spitler, L. R., Romanowsky, A. J., Diemand, J., et al. 2012, MNRAS, 423, 2177
Springel, V. 2005, MNRAS, 364, 1105
Starkenburg, E., Helmi, A., De Lucia, G., et al. 2013, MNRAS, 429, 725
Thoul, A. A., & Weinberg, D. H. 1996, ApJ, 465, 608
Trenti, M., Smith, B. D., Hallman, E. J., Skillman, S. W., & Shull, J. M. 2010, ApJ, 711, 1198
van den Bosch, F. C., & Ogiya, G. 2018, MNRAS, 475, 4066
Weisz, D. R., Dolphin, A. E., Skillman, E. D., et al. 2014, ApJ, 789, 148
Weisz, D. R., Dolphin, A. E., Skillman, E. D., et al. 2015, ApJ, 804, 136
Weisz, D. R., Martin, N. F., Dolphin, A. E., et al. 2019, ApJL, 885, L8
Wetzel, A., Hayward, C. C., Sanderson, R. E., et al. 2023, ApJS, 265, 44
Wheeler, C., Hopkins, P. F., Pace, A. B., et al. 2019, MNRAS, 490, 4447
White, S. D. M., & Frenk, C. S. 1991, ApJ, 379, 52
White, S. D. M., & Rees, M. J. 1978, MNRAS, 183, 341
Willman, B., Governato, F., Dalcanton, J. J., Reed, D., & Quinn, T. 2004, MNRAS, 353, 639
Wolf, J., Martinez, G. D., Bullock, J. S., et al. 2010, MNRAS, 406, 1220